ELSEVIER

Chemical Physics 207 (1996) 411–426

Chemical Physics

State specific, angle velocity resolved measurements of photodissociation in clusters: I atom escape from $(CH_3I)_n$ $(n = 1,2,3)$

Jack A. Syage *

The Aerospace Corporation, P.O. Box 92957, M5-754, Los Angeles, CA 90009, USA

Received 2 October 1995

Abstract

The photodissociation of molecules in clusters affords the opportunity to study collisional relaxation of translational and rovibrational energy under solvent-like conditions. We have measured the angle velocity distribution of $I(^2P_{3/2})$ and $I(^2P_{1/2})$ from photodissociation of $(CH_3I)_n$ clusters at 266 and 304 nm. For monomer ($n = 1$), the angular distributions are very anisotropic and the translational energy is sharply peaked at high energy. For clusters (predominantly $n = 2,3$), the dissociated I atom undergoes collisions, which substantially relax the translational energy and anisotropy. Three observations are reported: (1) A residual anisotropy exists in cluster photodissociation that increases with increasing translational energy. This observation is believed to reflect the correlation of anisotropy and energy loss due to the impact parameter and number of collisions of the photofragment in the cluster. Anisotropy versus kinetic energy plots maybe interpreted to give collisional relaxation rates in clusters. (2) The I atom $^2P_{3/2}$ to $^2P_{1/2}$ branching ratio increases significantly in clusters relative to the monomer. Possible explanations are discussed including increased adiabaticity through the curve-crossing region in dissociation due to cage effects in analogy with reported surface results. (3) TOF spectra were observed for I atoms originating from photodissociation of the cluster photoproduct I_2. The recorded spectra are consistent with an I_2 energy content that is much less than the initially excited $(CH_3I)_n$ cluster.

1. Introduction

Research in clusters holds the potential to learn about condensed phase properties at the state-to-state level with single molecule resolution. A burgeoning area of interest is the study of chemical dynamics in clusters. With regard to dynamical studies of clusters, the main pursuit in our group and elsewhere has been in time domain measurements of chemically reacting systems [1,2]. In the present work, we take a different approach toward measuring fast dynamics in clusters. We describe an experiment to measure collisional relaxation rates of translational, vibrational, and rotational energy in clusters. The method is based on photodissociating a molecule in a cluster and measuring the change in the nascent rovibrational and translational energy of the fragment as a function of residence time in the cluster. These properties are most directly measured in the time domain using a technique such as femtosecond ki-

* Corresponding author. Fax: +1 310 3367680; e-mail: jack_syage@qmail2.aero.org

PII 0301-0104(95)00438-6

netic energy time-of-flight spectroscopy introduced by the Zewail group [3]. In our case, we probe the angular distribution of the translational and internal energy spectrum using narrow band nanosecond pulses. The angular distribution may be interpreted in terms of fragment residence time in the cluster. The angle velocity distribution is also useful for obtaining geometry information on a cluster. In keeping with the topic of this special issue, "Laser and Molecular Beam Studies of Chemical Reaction Dynamics", we present evolving work to show the kind of information that can be obtained concerning cluster reaction dynamics. The objective is to identify important areas for study and to suggest avenues for solving some of the most immediate questions.

Soep, Jouvet, and coworkers [4] and Wittig and coworkers [5,6] have pioneered spectroscopic studies of reaction products from van der Waals molecules (we distinguish this chemistry from the more extensive studies of van der Waals dissociation). The former group studied a series of excited state dimer reactions of the type $HgX_2^* \rightarrow HgX^* + X$ ($X = Cl_2$, H_2) and measured product rovibrational distributions from dispersed fluorescence spectra of electronically excited HgX^*. Wittig's group measured OH and CO product internal energy distributions for CO_2–HX complexes (X = Cl, Br, and I) by laser induced fluorescence [5,6]. These complexes assume specific equilibrium geometries, that vary with X, providing the means to explore chemical dynamics for prealigned collision parameters. The complex reaction $H + CO_2$ forms OH + CO with a reaction efficiency and partitioning of energy into rotation and vibration that depends strongly on the bimolecular alignment. The groups of Zewail [7] and Wittig [6] have extended these experiments into the femtosecond time domain. Wittig has recently implemented a method for measuring the translational energy distribution for H atoms scattering out of complexes [8]. By exciting dissociated H atom to high n Rydberg states and field ionizing them at the detector, they have achieved very high velocity resolution (by avoiding space charge repulsion). They have measured angle velocity distributions for H atom scattering from the photoinitiated complexes Ar–HX (X = Br, I). These studies measure fundamental properties of solvent caging effects, which is also part of the motivation of the present work.

Product translational energy techniques are being applied to photoinitiated cluster reactions to measure energy partitioning. Cluster ion photodissociations have dominated these studies because ion fragments are convenient to detect [9]. However, the fragment ions are typically not detected in specific energy states. For neutral dissociation, the fragments must be probed, which is usually done in a state specific manner by resonance ionization or fluorescence detection. In studies of neutral CH_3I monomer photodissociation, Penn et al. [10] and Ogorzalek Loo et al. [11] observed that cluster formation broadens the time-of-flight spectrum for the I atom. The monomer dissociation is known to be very anisotropic with a velocity distribution sharply peaked at high energy. The product velocity distribution for the clusters, however, was broad and peaked at zero component velocity. In a preliminary account to the present work, we reported detailed measurements of the spin–orbit state dependent $^2P_{3/2}$ and $^2P_{1/2}$ I atom velocity distribution for $(CH_3I)_n$ cluster photodissociation [12]. Young has recently measured I atom and H atom translational energy spectra for $(CH_3)_n$ cluster photodissociation [13], the results of which are very relevant to the present discussion. In a different vein, the Miller group has applied the novel use of a strong electric fields to orient complexes such as N_2–HF for angle resolved measurements [14]. Using infrared lasers for state-to-state pump and probe, they vibrationally excite HF and then measure the angular distribution of N_2 and HF in specific rovibrational states by rotating the probe laser and bolometer detector with respect to the molecular axis.

The present work reports on the angular dependence of the I atom velocity distribution in the $^2P_{3/2}$ and $^2P_{1/2}$ state (henceforth I and I^*) following excitation of $(CH_3I)_n$ ($n = 1$–3) at 266 and 304 nm. These measurements lead to the angle dependent translational energy distribution and product branching ratio I/I^*. These studies probe cluster geometries and cage escape dynamics of I atom and, therefore, complement measurements of cage recombination in clusters and bulk phase. Ultrafast spectroscopy has recently been applied to measure I_2 recombination in rare gas clusters by the Zewail group [15] I_2^- recombination in CO_2 clusters by the Lineberger group [16], and I_2 recombination in rare

gas matrices by the Apkarian group [17]. The dissociated I atom in $(CH_3I)_n$ photolysis is known to undergo intracluster chemistry leading to I_2 formation, so the escape of I atom competes with I_2 formation [18–21]. The angle velocity resolved measurements of the I atom presented here are able to distinguish the nascent I atom escaping from the cluster from the I atom that dissociates *after* forming the intracluster product I_2. Young has also observed the I atom originating from product I_2 arising from photodissociation in $(HI)_2$ [13].

The formation of I_2 in $(CH_3I)_n$ cluster photodissociation has been an area of active interest. Vaida and coworkers first detected I_2^+ by multiphoton ionization of $(CH_3I)_n$ through the A state [18]. Our group presented picosecond mass selective measurements of $(CH_3I)_n$ A state photochemistry to confirm that I_2 was formed by a neutral cluster reaction [19]. Independent evidence was provided by Wang et al. [20] and Fan and Donaldson [21] who measured the vibrational distribution of the I_2 product. The former investigators measured a vibrational temperature of about 1000 K for 200 nm photolysis. The latter work at 193 and 248 nm photolysis, however, is consistent with a rovibrational distribution having an upper limit of 300 K. We will discuss these results in greater detail in the Section 5.

2. Model for measuring differential cross sections

2.1. Concept

The detection geometry for measuring angle resolved time-of-flight (TOF) spectra is illustrated in Fig. 1. The fragment 3D spatial distribution expands as it travels down the drift tube to the detector. The sphere in Fig. 1 represents a surface of ions of velocity or speed v. An aperture placed in front of the detector limits the field-of-view to a cylinder of ions of maximum radial velocity $\delta_r = r/t_0$ where r is the effective aperture radius, and t_0 is the ion packet drift time. The angular and velocity resolutions are dependent on photofragment speed v and are given by

$$\Delta\theta_z = \arcsin(\delta_r/v) \text{ (angular resolution)}, \quad (1)$$

$$\Delta v/v = 1 - (v_{z,\min}/v) = 1 - \cos(\Delta\theta_z) \text{ (velocity resolution)}. \quad (2)$$

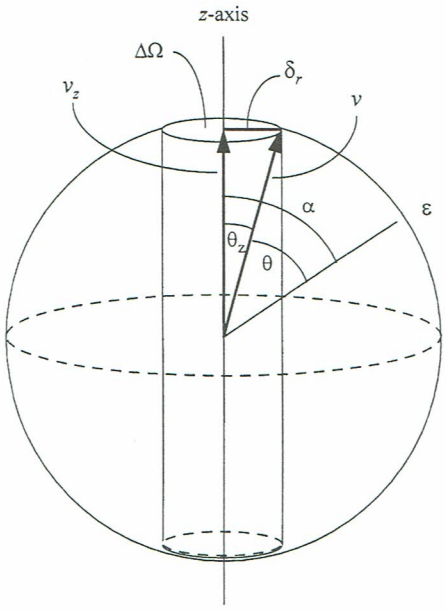

Fig. 1. Geometry for product recoil and detection cylinder. Parameters are described in the text.

The detection cylinder limits the angular range of fragment of velocity v thereby limiting the width of the v_z projection. This defines the velocity resolution Δv. As δ_r decreases relative to v, the detected v_z distribution becomes a good measure of the speed distribution v. In the present work, we probe through the center of the ion 3D velocity distribution at different angles α. In previous work, we recorded series of 1D TOF spectra by sequentially offsetting the detection cylinder from centerline, thereby mapping out a 2D section of the 3D velocity distribution [16].

2.2. General equations

The differential cross section for photodissociation with respect to fragment speed v and recoil solid angle Ω is given by

$$\frac{d^2\sigma}{d\Omega\, dv} = \frac{d\sigma}{d\Omega} g(v) = \frac{1}{4\pi}\left[1 + \beta(v) P_2(\cos\alpha) P_2(\cos\theta_z)\right] g(v). \quad (3)$$

The separation of the angular and velocity distributions is strictly valid for collisionless photodissociation, but less valid for cluster photodissociation where collisions affect the angle velocity distributions. In the limit of multiple collisions or long lifetime cluster residence times leading to an isotropic distribution, $g(v)$ becomes independent of the angle once again. In Eq. (3), we have transformed to the laboratory drift tube z-axis where $d\Omega = \sin\theta_z\, d\theta_z\, d\varphi_z = 2\pi \sin\theta_z\, d\theta_z$ is the laboratory frame solid angle. The angle θ is the fragment recoil angle relative to the electric field axis ε and α is the angle of ε relative to the z-axis. Hence the photofragment recoil angle relative to the z-axis is $\theta_z = \theta + \alpha$. The second Legendre polynomial is defined as $P_2(x) = (3x^2 - 1)/2$ and β is the anisotropy factor for the angular distribution. The maximum anisotropies for parallel and perpendicular transitions are 2 and -1, respectively, and a value of 0 corresponds to an isotropic angular distribution.

The flux of ions along the z-axis per unit time with radial velocity v_r is given by

$$\frac{d^2N}{dt\,dv_r} = \kappa \frac{d\sigma}{d\Omega} g(v) \left(\frac{d\Omega}{dv_z} \frac{dv_z}{dt} \frac{dv}{dv_r} \right), \tag{4}$$

where the following identities are defined as

$$\frac{d\Omega}{dv_z} = \frac{-2\pi}{v}, \quad \frac{dv_z}{dt} = \frac{qE}{m}, \quad \frac{dv}{dv_r} = \frac{v_r}{v}. \tag{5}$$

The evaluation of $d\Omega/dv_z$ follows from Fig. 1 and dv_z/dt is obtained under space focusing conditions where q is ion charge, E is the ion drift energy, and m is ion mass. Under non-space focusing conditions, dv_z/dt is a complicated function. The κ term encompasses a set of constants that includes laser intensity, molecular beam density, ionization efficiency, detection sensitivity, etc.

The observed TOF spectrum $I(v_z)$ is obtained by integrating over the area of the detection aperture. Ideally, the detection efficiency $\eta(v_r)$ as a function of the radial velocity v_r, is described by a step function. However, the ion packet that is imaged onto the detection aperture can potentially have some blurring due to deflection off the grids in the acceleration region (see Section 3). In this general case, the TOF spectrum is described by

$$I(v_z) = \int_0^\infty \frac{d^2N}{dt\,dv_r} \eta(v_r)\, dv_r$$

$$= \kappa \int_0^\infty \frac{d\sigma}{d\Omega} \frac{g(v)}{v^2} \eta(v_r)\, v_r\, dv_r. \tag{6}$$

If we assume a step function detection efficiency such that $\eta(v_r) = 1$ or 0 for v_r less than or greater than the aperture radius δ_r, respectively, then Eq. (6) simplifies to

$$I(v_z) = \kappa \int_0^{\delta_r} \frac{d\sigma}{d\Omega} \frac{g(v)}{v^2} v_r\, dv_r. \tag{7}$$

It is sometimes convenient to integrate over v by the change of variables $v_r dv_r = v dv$ to give

$$I(v_z) = \kappa \int_{v_{min}}^{v_{max}} \frac{d\sigma}{d\Omega} \frac{g(v)}{v}\, dv, \tag{8}$$

where $v_{min} = v_z$ and $v_{max} = (v_z^2 + \delta_r^2)^{1/2}$. These limits represent the range of v values that can project to a specific value of v_z.

2.3. Core sampling

The condition for core sampling is $\delta_r \ll v$, which leads to the relation $v_z \approx v$. If $g(v)$ is a slowly varying function over dv_r, then Eq. (7) simplifies to

$$I_\alpha(v_z) = \kappa \frac{\delta_r^2}{2v_z^2} \frac{d\sigma}{d\Omega_\alpha} g(v). \tag{9}$$

This leads to the important conclusion that the differential cross section for fragment scattering angle $\theta = \alpha$ is directly measurable and that $g(v)$ is obtained as a consequence. When $\delta_r \ll v$ is not satisfied, such as when v is small, v_z ceases to be a good measure of v. Then the integral in Eq. (7) or (8) must be carried out explicitly in order to fit a calculated $I(v_z)$ to observed measurements. It is important to note that the derivations leading to Eq. (9) do not require the assumption of separability of the angular and velocity distributions. $I_\alpha(v_z)$ is a valid measure of the coupled differential cross section $d^2\sigma/d\Omega_\alpha dv$.

Calculated TOF spectra for various cases of v and

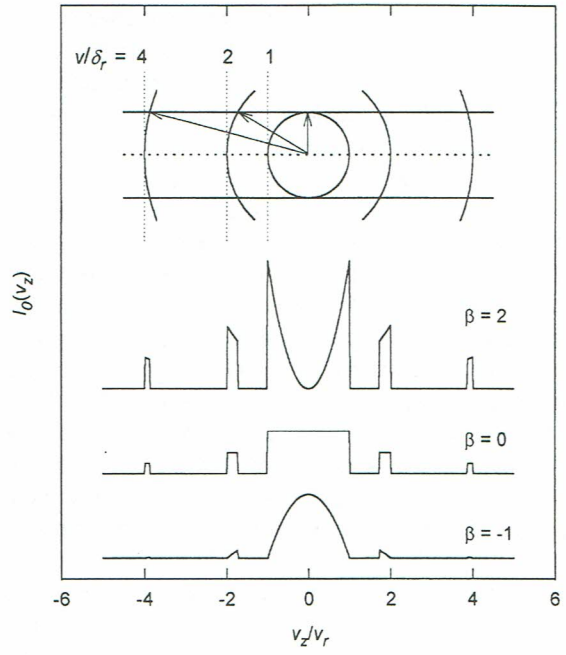

Fig. 2. Calculated TOF spectra for delta function velocity distributions as a function of radial resolution δ_r.

δ_r, ranging from core sampling to 1D projections are presented in Fig. 2. For $v/\delta_r \leq 1$, a pure 1D projection is observed. Interestingly, v/δ_r does not have to become very large for accurate core sampling measurements of $g(v)$ to be obtained. The case for $v/\delta_r = 4$ in Fig. 2 corresponds to a $\Delta v/v$ of 0.03 (Eq. (2)).

2.4. Fitting g(v) distributions

The core sampling conditions described above break down as $v \rightarrow 0$. For direct dissociations where the velocity distributions are highly peaked, there may be very little ion flux at low v where the core sampling conditions are invalid. In this case, a direct determination of the differential cross section is possible. Otherwise, low v distributions should be fitted to a trial $g(v)$ distribution.

Velocity distributions $g(v)$ are most conveniently obtained from centerline core sampling TOF spectra $I_\alpha(v_z)$. Fits are obtained by adding calculated $I_v(v_z)$ TOF for individual increments of v using a trial function $g(v)$. Formally it is described by the operation

$$I_\alpha(v_z) = \kappa \int_0^\infty \frac{d\sigma}{d\Omega_\alpha} \frac{g(v)}{v} \eta_v(v_r)\, dv$$

$$= \frac{\kappa}{v} \frac{d\sigma}{d\Omega_\alpha} \sum_v g(v)\eta_v(v_r)\Delta v, \qquad (10)$$

which is similar to Eq. (8) except that we have used a generalized function $\eta_v(v_r)$ rather than a step function for the radial resolution (aperture function). It is still useful to use a radial step function, which would then give the convenient limits of integration of Eq. (8). It is also possible to fit experimental spectra to Eq. (6) or (7), in which case $I_\alpha(v_z)$ is composed of a sum of TOF spectra for increments of v_r (i.e., $I_{vr}(v_z)$) and summed over the weighing function $\eta(v_r)$.

An important simplification occurs when $\beta = 0$ and $g(v)$ can be described by a Maxwell–Boltzmann distributions (i.e., $g(v)dv = \exp(-v^2/\sigma_v^2)\, v^2 dv$, where σ_v is the Gaussian width). Eq. (8) becomes

$$I(v_z) = \kappa \int_{v_{min}}^{v_{max}} e^{-v^2/\sigma_v^2} v\, dv$$

$$= \frac{\kappa \sigma_v^2}{2} e^{-v_z^2/\sigma_v^2}\left(1 - e^{-\delta_r^2/\sigma_v^2}\right). \qquad (11)$$

Eq. (11) describes the interesting property of isotropic Maxwell–Boltzmann distributions that any 1D cylindrical slice of the 3D Gaussian distribution gives the same shaped curve for $I(v_z)$. The relation $v_z^2 I(v_z) \propto g(v)$ is, therefore, equally valid for 1D projection and core sampling conditions.

2.5. Translational energy distributions

The probability distribution for fragment translational energy is obtained from the relation $P(E)dE = g(v)dv$, which gives $P(E) = g(v)/mv$. Under core sampling conditions, Eq. (9) leads to

$$P(E_t) = \left(\kappa m \delta_r^2 \frac{d\sigma}{d\Omega_\alpha}\right)^{-1} v_z I_\alpha(v_z), \qquad (12)$$

where $E_t = mv_z^2/2$ is fragment kinetic energy and the terms in parentheses are constants. For an isotropic Maxwell–Boltzmann distribution, $P(E_t) \propto v_z I_\alpha(v_z)$ regardless of the radial resolution v_r. The c.m. translational energy is computed from

$$E_{t,c.m.} = E_t\left(\frac{M}{M-m}\right), \tag{13}$$

where m is the detected fragment mass and M is the molecular precursor mass.

3. Experimental

Details of our experimental apparatus for measuring angle velocity distributions has been described before [12,22]. A schematic of our time-of-flight mass spectrometer is given in Fig. 3 and consists of an ion optics assembly of three grids separated by 1 cm, a one meter drift tube, and a 5 mm diameter aperture mounted in front of an 18 mm diameter microchannel plate detector. The results presented here were collected using 30 and 480 V/cm for the extraction and acceleration fields, respectively. Under these operating conditions, I^+ ions have flight times centered at $t_0 = 42$ μs. Space focusing conditions were estimated from calculations and then optimized by adjusting the extraction voltage until the ion TOF time was invariant to movement along the z-axis of the ionization volume in the molecular beam. A combination of the detector aperture diameter and blurring of the ion image due to diffraction off grids currently limits our spatial resolution to about 10 mm, corresponding to a radial resolution of $\delta_r = 0.12$ km/s. We have operated at higher resolution ($\delta_r < 0.1$ km/s) in earlier work on the CH_3I monomer [22], and with planned improvements we should be able to achieve the same resolution in future cluster measurements.

Photolysis was initiated at 266 and 304 nm. I and I^* photofragments were ionized by 2 + 1 resonance enhanced multiphoton ionization (REMPI) using excitation at 304.7 nm ($^6P^2D^0_{5/2}$ intermediate state) and 304.0 nm ($^6P^4D^0_{1/2}$ state), respectively. For 266 nm photolysis, the pump pulse precedes the probe pulse by about 10 ns. For 304 nm photolysis, the pump and probe pulses are the same. The laser polarization angle α of the pump was varied by rotating a combination of a double Fresnel–Rhomb and a Glan–Taylor polarizer. Flat windows were used on the molecular beam port to minimize polarization dependent transmission. The incident pump and probe laser pulse energies were measured using a photodiode at the exit window of the molecular beam. Laser pulse energies and focusing conditions were adjusted to avoid space charge repulsion and in the case of 266 nm photolysis to maximize the two-pulse signal relative to the one-color signal. TOF spectra were collected using a LeCroy 9450 digital scope.

The CH_3I sample was placed in a bubbler cooled to 0°C and delivered to the pulsed valve by a flow of Ar at 1000 Torr (results were unchanged at lower temperatures). To reduce cluster formation, the pulsed valve was heated to 60°C. Near cluster-free monomer TOF spectra could be obtained by synchronizing laser excitation to the leading edge of the gas pulse. Increasing amounts of cluster signal could

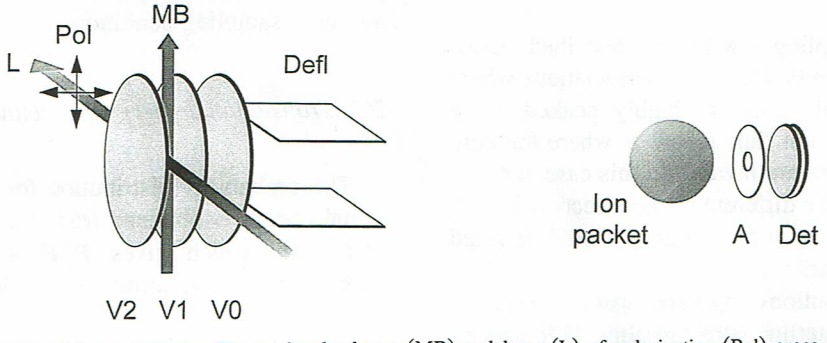

Fig. 3. Schematic diagram of the experiment. The molecular beam (MB) and laser (L) of polarization (Pol) cross perpendicularly in the acceleration region (V1–V2) of a TOF mass spectrometer. Deflector plates (Defl) center the ion packet across the aperture (A) placed in front of the detector (Det). Drawing is not to scale.

be obtained by moving the laser excitation toward the peak of the gas pulse.

The present core sampling technique is similar to that developed by the groups of Houston [23], El-Sayed [24] and Chandler [25]. These investigators use delayed ion extraction to achieve large separation of the velocity components, but the non-space focusing conditions complicate the relationship between v_z and $t - t_0$. We have opted for space focusing conditions because of the linear relation between v_z and $t - t_0$ as discussed earlier.

4. Results and analysis

Photofragment TOF spectra of $I(^2P_{3/2})$ and $I(^2P_{1/2})$ were recorded for monomer and cluster photodissociation of CH_3I at 266 and 304 nm. Observed TOF traces $I_0(v_z)$ and $I_{90}(v_z)$ are presented in Fig. 4 for the $I(^2P_{3/2})$ photofragment for 266 nm photolysis. The series of Figs. 4a,a′ to 4c,c′ represent conditions of increasing clustering. Calculated curves are fitted to the data in Fig. 4. The curve fits to the monomer results were calculated using a previously determined $g(v)$ distribution convolved with the instrument function $\eta_v(v_r)$ for the present experiments according to Eq. (10). The curve fits to the cluster results were calculated from a single Gaussian function. The following observations in Fig. 4 are evident: (1) with increasing clustering, a broad peak centered at $v_z = 0$ emerges, that scatters 0° and 90° relative to ε, and (2) for cluster photodissociation, the width of the $I_{90}(v_z)$ distribution is narrower than for the $I_0(v_z)$ distribution.

The observed TOF spectra are believed to be due predominately to photodisscsiation of dimer with some

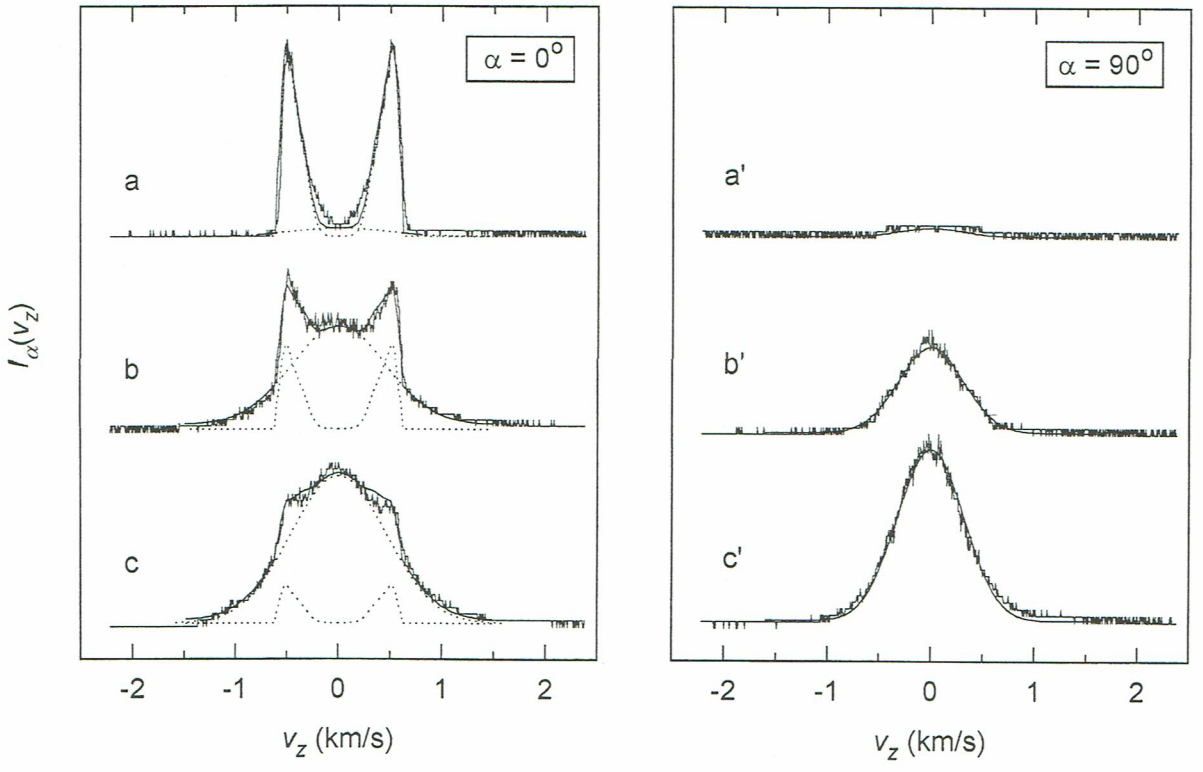

Fig. 4. Angle resolved $I(^2P_{3/2})$ photofragment velocity distributions $I_\alpha(v_z)$ for $(CH_3I)_n$ excitation at 266 nm where α is the alignment of v relative to the drift tube z-axis and $\theta = \alpha$ is the product recoil angle relative to ε. (a,a′) monomer excitation, (b,b′) monomer and cluster excitation, (c,c′) increasing cluster distribution. Calculated fits are shown (————) along with the individual contributions due to monomer and cluster excitation (· · ·). The $I_\alpha(v_z)$ spectra were fitted to Gaussian functions of the form $\exp\{-v_z^2/\sigma_v^2\}$ where σ_v^2 is 0.65 km/s and 0.45 km/s for $\theta = 0°$ and 90°, respectively.

contribution to trimer. The main evidence is that the shape of the $I_\alpha(v_z)$ distributions in Fig. 4 attributable to clusters does not change as conditions for clustering are increased. Hence, if the first indication of clustering is due to dimers and some trimers, then it is reasonable to conclude that dimers and trimers dominant under increasing clustering conditions. Other evidence supporting this conclusion is previous work in our group using low-energy electron impact ionization of $(CH_3I)_n$ in which a decreasing cluster size distribution was always observed, regardless of the intensity of the clustering conditions [19,26].

Fragment translational energy distributions $P(E)$ for monomer and cluster photodissociations were evaluated from the $I_0(v_z)$ and $I_{90}(v_z)$ fits and are plotted in Fig. 5. The velocity dependent anisotropy in Fig. 4 is clearly evident in Fig. 5. Interestingly, $P(E)$ is well described by a Maxwell–Boltzmann distribution despite the anisotropy. As it is not possible to ascertain the proportion of the $I_\alpha(v_z)$ that are due to dimers versus trimers, we evaluate $\langle E_{t,c.m.} \rangle$ in Table 1 assuming one or the other cluster size in order to place boundaries on the translational energy distributions. Assuming two-body dissociation of dimers, the translational energies correspond to temperatures of 5700 and 2700 K for $\theta = 0°$ and 90° fragment recoil, respectively.

In a preliminary account of this work, we presented c.m. translational energy distributions assuming a two-body dissociation [13]. The observation that E_t can be greater in cluster dissociation than monomer dissociation argues that two-body dissociation is occurring. As such, the translational energy distribution is plotted in the c.m. frame in Figs. 5b and 5c (assuming two-body dimer dissociation). However, the multimodal nature of the velocity distribution may also be evidence of a many-body dissociation. We consider these issues in Section 5. Similar observations have been reported for surface adsorbed CH_3I, where the photodissociated I atom can acquire translational energy greater than is allowable by kinematic constraints in an isolated gas phase molecule according to Eq. (13) [27,28]. The explanation given in the surface studies is that the high velocity CH_3 can impart velocity to I atom by a "chattering" type multiple collision interaction.

The cluster results for 304 nm photolysis in Figs. 6 and 7 are similar to the 266 nm results with respect to the general appearance of the monomer and cluster TOF traces, aside from the lower recoil velocity for the longer wavelength. However, the 304 nm cluster results are markedly bimodal. The bimodal distribution is reasonably well fit by the sum of two Gaussian functions. The 266 nm results in Fig. 4c would also be better fit to a bimodal distribution.

Table 1
Mean translational energy releases and spin–orbit branching ratios for $(CH_3I)_n$ photodissociation

Photolysis wavelength (nm)	Excess energy (kcal/mol)	n	Fragment translational energy $\langle E_t \rangle$ (kcal/mol) [a]		c.m. translation energy $\langle E_{t,c.m.} \rangle$ (kcal/mol)		Branching ratio
			$\theta = 0°$	$\theta = 90°$	$\theta = 0$	$\theta = 90°$	
$(CH_3I)_n \rightarrow I(^2P_{3/2})$							
266	54.4	1	4.8	–	45	–	0.37 [c]
		2, 3	9.4	–	13–17	–	0.8
			4.5 [b]	4,5	6–8	6–8	
304	41.0	1	3.6	–	34	–	1.1
		2, 3	11.9	–	16–21	–	> 2.0
			2.5 [b]	2–5	3–5	3–5	
$I_2(CH_3I)_n \rightarrow I(^2P_{3/2})$							
304	36.0 [d]	0	–	17.8	–	33.6	1.0
		> 0	–	10.6	–	21.3	

[a] Range of values depends on the assumption of $n = 2$ versus $n = 3$. See captions to Figs. 4 and 6.
[b] Two sets of energies represent bimodal distribution; high-energy component is much less evident at $\theta = 90°$ than is the low-energy component.
[c] Ref. [27].
[d] Assumes I–I dissociation energy of 36.5 kcal/mol and a dissociative limit of I + I * (excited spin–orbit energy of 21.6 kcal).

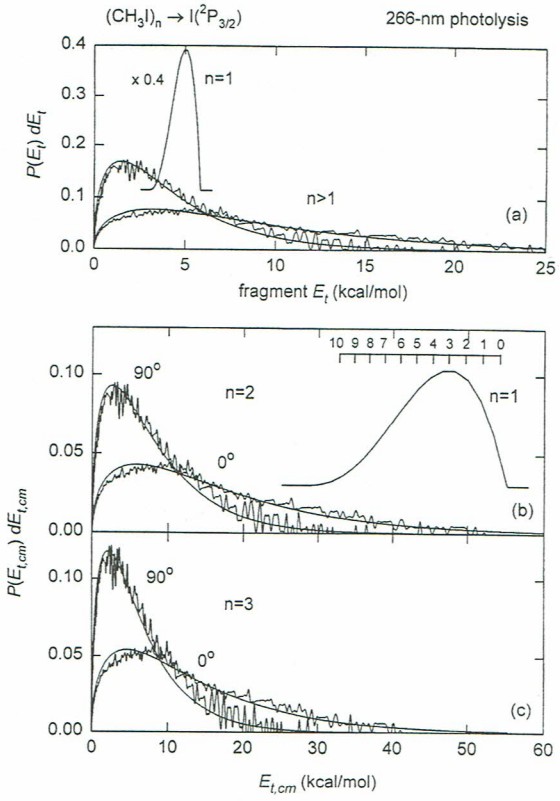

Fig. 5. (a) Fragment and (b), (c) c.m. translational energy distribution for $(CH_3I)_n$ excitation at 266 nm and $I(^2P_{3/2})$ dissociation. Curves were obtained from the calculated $g(v_z)$ fits to $I_\alpha(v_z)$ in Fig. 4. The vibrational energies for the CH_3 ν_2 mode are shown for $n=1$. The $n=2$ and $n=3$ results in (b) and (c) represent how the calculated $P(E_{t,c.m.})$ are affected by assuming dissociation from dimer versus trimer. Each curve is normalized to $\int P(E)\,dE = 1$. See Table 1 for $\langle E_t \rangle$ values.

An additional velocity component that is peaked at high velocity and is anisotropic appears in Fig. 8b. This signal can be assigned to I_2 photodissociation on the basis of conservation of energy $E_t = h\nu - D_0 - E_{int}$ where $h\nu$ is the photon energy (4.08 eV), D_0 is the bond dissociation energy, which is 1.58 eV for I_2 (2.30 eV for CH_3I), and E_{int} is the internal energy of the counter fragment, which is 0 or 0.94 eV for I or I^*, respectively. The I atom signal due to I_2 has a higher order dependence on laser power than do the other I atom signals, which have the same dependence on laser power. This result is inconsistent with I atom coming from I_2 impurity, but rather from dissociation of I_2 that originated as a photoproduct from $(CH_3I)_n$ excitation. Young reported evidence of I atom originating from an I_2 photoproduct for $(HI)_n$ cluster photodissociation [13]. He carried out a thorough series of laser power dependence measurements to confirm that one component of the I^+ TOF signal is due to the I_2 cluster photoproduct.

Translational energy distributions are plotted in Fig. 7 for $I(^3P_{3/2})$ photodissociated from CH_3I and in Fig. 8c for photodissociated I_2 as isolated

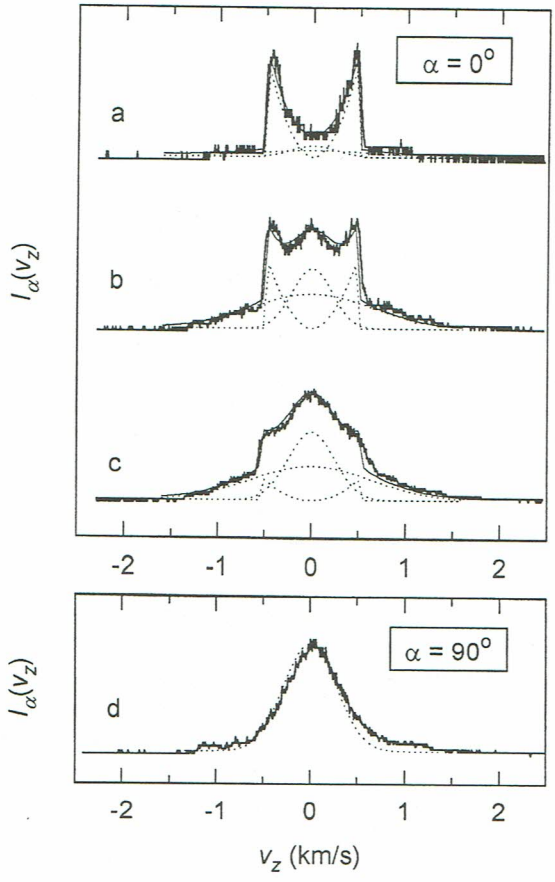

Fig. 6. $I_0(v_z)$ velocity spectra for $(CH_3I)_n$ excitation at 304 nm and $I(^2P_{3/2})$ detection as a function of increasing clustering conditions from (a) to (c). (d) $I_{90}(v_z)$ velocity spectra under clustering conditions. Calculated fits are shown (————) along with the individual contributions due to monomer and cluster excitation (· · ·). The cluster contribution was fitted by two Gaussian functions $\exp(-v_z^2/\sigma_i^2)$ of widths $\sigma_i^2 = 0.75$ and 0.35 km/s.

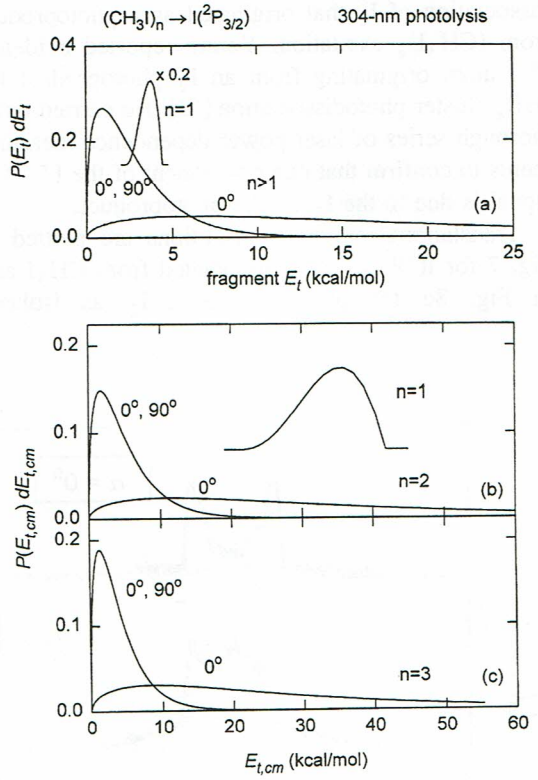

Fig. 7. (a) fragment and (b),(c) c.m. translational energy distribution for $(CH_3I)_n$ excitation at 304 nm and $I(^2P_{3/2})$ dissociation. Curves were obtained from the calculated $g(v_z)$ fits to $I_\alpha(v_z)$ in Fig. 6. The $n=2$ and $n=3$ results in (b) and (c) represent how the calculated $P(E_{t,c.m.})$ are affected by assuming dissociation from dimer versus trimer. Each curve is normalized to $\int P(E)\,dE = 1$. See Table 1 for $\langle E_t \rangle$ values.

molecules and in complexes. The I atom $P(E)$ distribution from 304 nm photolysis of $(CH_3I)_n$ is anisotropic as it is for 266 nm photolysis (Fig. 4 and Fig. 5). However, the bimodal distribution at $\alpha = 0°$ is more evident at 304 nm, showing distinct fast and slow Maxwell–Boltzmann distributions (Fig. 6 and Fig. 7). At $\theta = 90°$ recoil angle, the fast component is much reduced in intensity relative to the slow component. The $P(E)$ distribution for these individual components is plotted in Fig. 7. The I atom velocity distribution originating from the I_2 photoproduct is also bimodal, however, this can be attributed to complexed and uncomplexed I_2. The sharp high velocity feature in Fig. 8b is anisotropic with a value $\beta < 0$ that indicates a perpendicular transition, and has a $P(E)$ distribution, shown in Fig. 8c, that corresponds to the dissociative limit $I + I^*$. This is consistent with the photodissociation properties of I_2 in the ultraviolet [29]. We assign this signal to dissociation of uncomplexed I_2 photoproduct. Another component is observed that has a broader $P(E)$ distribution, but is still anisotropic and non-Maxwell–Boltzmann that can be assigned to dissociation of I_2 complexed to CH_3I.

A velocity dependent anisotropy is calculated from the relation

$$\beta(v) = \frac{I_0(v_z) - I_{90}(v_z)}{\frac{1}{2}I_0(v_z) + I_{90}(v_z)} \qquad (14)$$

Because $I_0(v_z)$ and $I_{90}(v_z)$ are well-described by Gaussian functions, $\beta(v_z)$ also has a Gaussian shape, both calculated and observed as seen in Fig. 9.

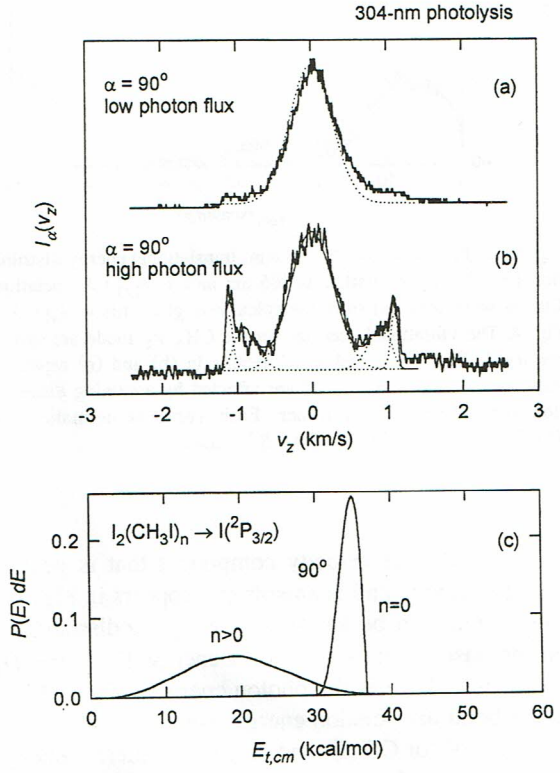

Fig. 8. (a), (b) $I_{90}(v_z)$ velocity spectra for $(CH_3I)_n$ excitation at 304 nm and $I(^2P_{3/2})$ detection as a function of photon flux. Calculated fits are shown (————) along with the individual contributions due to monomer and cluster excitation (· · ·). (c) c.m. translational energy distributions for I_2 precursors to detected I atom. Each curve is normalized to $\int P(E)\,dE = 1$. See Table 1 for $\langle E_t \rangle$ values.

Measurements were made of the relative yields of I and I* from monomer and cluster photodissociation. 2 + 1 REMPI excitation spectra of I atom were recorded over the wavelength range 303 to 305 nm, which encompasses three strong $^2P_{3/2}$ transitions and one $^2P_{1/2}$ transitions. We show two transitions in Fig. 10. Pure monomer photofragment spectra were collected by detecting the entire TOF spectrum for $\theta = 0°$ recoil under non-clustering conditions (e.g., in Fig. 4a). Pure cluster photofragment spectra were recorded by detecting the TOF spectrum at $\theta = 90°$ recoil under clustering conditions (e.g., in Fig. 4c′). From the ratio of the I and I* signals and the known branching ratio for monomer at 266 nm [30], it was possible to determine the branching ratios reported in Table 1. The significant observation is that the spin–orbit state distribution is greatly relaxed in cluster dissociation.

An effect that we did not explore in these studies is whether the electronic angular momentum of the I atom is strongly coupled to the dissociation. This so-called electronic ***v–j*** correlation is observable by an anisotropy that varies with the polarization of the probe laser. The magnitude of the effect might also be spin–orbit state dependent. For the two-color 266 nm pump, 304 nm probe measurements, the probe polarization was fixed in the laboratory frame for both $\alpha = 0°$ and 90° probe polarization. For the one-color 304 nm pump and probe measurements, the polarizations of both pulses were the same. Essentially similar behavior was observed for 266 and 304 nm pump excitation, leading us to believe that the measured anisotropies are not strongly dependent on probe polarization. However, this effect deserves further attention. Of some interest is whether ***v–j*** correlation is collisionally quenched in cluster versus monomer photodissociation. There may also be a ***v–j*** correlation involving the rotational angular momentum of the CH_3 fragment. We hope to explore this property in future experiments involving CH_3 detection.

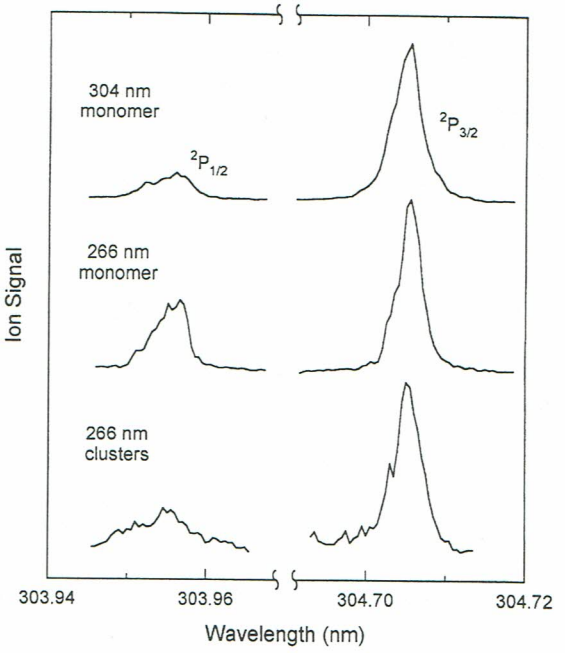

Fig. 10. Comparison of 2+1 REMPI signals for the $^2P_{1/2}$ and $^2P_{3/2}$ spin–orbit states of the I atom through the $^6P^4D^0_{1/2}$ and $^6P^4D^0_{5/2}$ intermediate states, respectively. Spectra are the sum of typically four scans. (Asymmetries in lineshapes are due to slight offsets in the addition of peaks.)

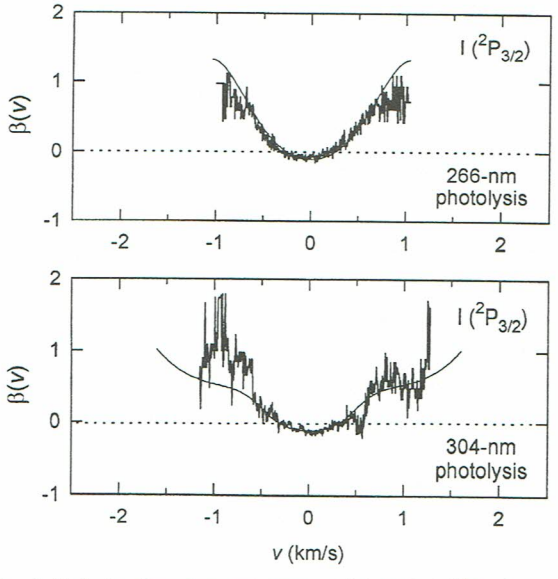

Fig. 9. Velocity dependent anisotropy $\beta(v)$ of the I($^2P_{3/2}$) fragment by 266 and 304 nm photolysis in $(CH_3I)_n$. The observed and calculated curves were obtained by plotting the measured and fitted $I_\alpha(v_z)$ data according to Eq. (14).

5. Discussion

We discuss four main results: (1) the anisotropy in the fragment velocity distribution including the

bimodal velocity distribution observed at $\alpha = 0°$ for 304 nm photolysis, (2) information gained about the dimer geometry, (3) the measured I atom velocity distribution from I_2 photoproduct dissociation, and (4) the relaxation of the spin–orbit state distribution in cluster versus monomer photodissociation.

5.1. Velocity dependent anisotropy

The measure of photofragment angle velocity (v,θ) distributions as a function of increasing cluster size n, probes events ranging from collisionless direct dissociation $(n = 1)$, to near single collision scattering $(n = 2)$, to multiple collisional relaxation $(n > 2)$. Direct dissociation for $n = 1$ is clearly evident from the highly anisotropic and peaked velocity distribution (Fig. 4a), a result observed many times in the past [31].

For cluster photodissociation, the anisotropy in the fragment velocity distribution may be understood as a collisional relaxation phenomena. Dissociated I atoms that have undergone few if any collisions in the complex will have an angle velocity distribution approaching the highly peaked and anisotropic distribution observed for monomer photodissociation. As the residence time and number of collisions in the complex increase, the fragment will lose energy and anisotropy. In the limit of many collisions, one might expect a velocity distribution that is approximately Maxwell–Boltzmann, with the lowest energy fragments being completely isotropic. Loss of I atom anisotropy could be due to residence times in the cluster on the order of a rotational period, or due to angle deflecting collisions. If the former property is significant, then the translational energy collisional relaxation rate may be determinable from E_t versus t plots, where t is obtained from β by relations for the rotational correlation function. The use of β as a rotational clock for molecules has been demonstrated by Hwang and El-Sayed [24].

5.2. Dimer geometry

An alternative picture to the above multiple collision fragment escape viewpoint is to assume the fragment (θ,v) distribution reflects scattering in a dimer and that the loss of anisotropy is due to a distribution of impact parameters to give a broad angular scattering distribution. This interpretation is probably the most relevant to the present work given the evidence for the predominance of dimers in the cluster distribution. The I atom (θ,v) distribution is a sensitive function of geometry. The $(CH_3I)_2$ dimer geometry is an issue of considerable interest. The formation of photoproduct I_2 argues for an I $\cdots$ I head-to-head geometry, however, there has not been conclusive evidence that I_2 forms in clusters as small as dimer. This work is consistent with an I_2 that forms from a dimer, thus supporting head-to-head bonding.

Wang et al. calculated the intermolecular potential for the $(CH_3I)_2$ dimer assuming three different relative alignments; collinear head-to-head, collinear head-to-tail, and side-on head-to-tail [20]. Only for the first alignment was a significant well observed (612 cm^{-1}), which they attribute to the iodine polarizability. When full geometry optimization was performed, a bent structure gave the greatest stability (1380 cm^{-1} well depth). The bent structure corresponds has calculated C–I $\cdots$ I bond angles of 175° and 115° and an intermolecular I $\cdots$ I bond length of 3.0 Å. Our experimental observations are consistent with this structure. Cleavage of the C–I bond aligned nearly collinear (175°) to the adjacent I atom would give a low impact parameter collision resulting in a relatively isotropic, low v distribution, whereas the more bent C–I $\cdots$ I bond (115°) would give a high impact parameter glancing collision resulting in a relatively anisotropic, higher v distribution. These trends are observed in this paper.

It must be cautioned that the bimodal velocity distribution can have other explanations. One possibility is that they represent different cluster sizes, namely $n = 2$ and $n = 3$. Even if trimers are formed in much lower abundance than dimers, a red-shift for trimer absorption relative to the dimer may enhance its excitation efficiency in the absorption wing at 304 nm. A second explanation is that the higher energy $P(E)$ component is due to direct dissociation to $I(^2P_{3/2})$ and the low energy distribution is due to dissociation to $I(^2P_{1/2})$ that undergoes a collisional relaxation to $^2P_{3/2}$. Collisional quenching of electronically excited states of atoms can be very efficient [32]. We plan to record a more complete set of data for the $I(^2P_{1/2})$ fragment to assess this possibility. Likewise, as a stronger test of the geometry, we

plan to measure the angular distribution of the CH_3 fragment.

It is interesting to compare the present results with the translational energy measurements reported for $(HI)_2$ cluster photodissociation by Young [13]. The I atom translational energy spectra were significantly broadened and strongly perturbed when operating under expansion conditions that increasingly favored cluster formation. On the other hand, the H atom translational energy spectrum was only negligibly affected by the same changes in expansion conditions. In that work, the dimer was assumed to form a H–I hydrogen bond (i.e., head-to-tail structure). Yet the H atom translational energy spectrum is more consistent with a H atom that points away from the intermolecular bond (i.e., I · · · I head-to-head structure). Young has discussed the possible geometries of $(HI)_2$, which are known only from theory. The most stable form is calculated to be L-shaped with a linear hydrogen bond, in analogy with the known structures of the other $(HX)_2$ hydrogen halide dimer geometries [33]. The inequivalent HX molecules in the dimer undergo tunneling with a splitting that increases with increasing halide mass. It is also known that the hydrogen bond strength decreases with increasing halide mass and that the dispersion force between halide atoms increases with halide mass. All these features suggest that a stable I · · · I bond in the $(HI)_2$ is plausible. In $(CH_3I)_2$ dimer, the hydrogen bond interaction is absent making the head-to-head alignment a likely structure.

5.3. I_2 product formation and subsequent photodissociation

The detection of I atom signal that can be positively assigned to dissociation of neutral I_2 photoproduct suggests a number of interesting properties of chemistry in $(CH_3I)_n$ clusters: (1) I_2 is formed in relatively high yield, even in small clusters of size $n = 2$ and 3. This property is also observed for $(HI)_n$ [13]. (2) The very sharp onset in the $I_2 \rightarrow I$ signal at $v_z = 1.2$ km/s in Fig. 8b is consistent with an I_2 energy (translational and rovibrational) that is much less than that for I atoms that escape the $(CH_3I)_n$ clusters. As noted earlier, Wang et al. measured a vibrational temperature of 1000 K for I_2 product from $(CH_3I)_n$ photodissociation [20]; however, Fan and Donaldson assert an upper limit of 300 K [21]. Both measurements are less than the Maxwell–Boltzmann translational temperatures that range from 2000–6000 K, as summarized in Table 1. For $(HI)_n$ photodissociation, Young reported I_2 TOF spectra that were unbroadened. We plan a similar measurement for $(CH_3I)_n$ to determine the source of cooling of I_2. One obvious explanation is evaporation of CH_3I to leave bare I_2.

The mechanism of I_2 formation is still a matter of uncertainty. Many groups have offered explanations [18–21]. There are two classes of mechanisms to consider. The first is a sequential mechanism involving photolytic bond breakage and bimolecular reaction

$$[CH_3 + I \cdots ICH_3] \rightarrow I_2 + 2CH_3, \quad \Delta H = 0.71 \text{ eV for I}, \tag{15a}$$

$$[CH_3 + I \cdots ICH_3] \rightarrow I_2 + 2CH_3, \quad \Delta H = -0.23 \text{ eV for I}^*, \tag{15b}$$

$$[CH_3 + I \cdots ICH_3] \rightarrow I_2 + C_2H_6, \quad \Delta H = -3.10 \text{ eV for I}. \tag{15c}$$

The second is a concerted photolytic mechanism

$$[CH_3I \cdots ICH_3] + h\nu \rightarrow I_2 + 2CH_3, \quad \Delta H = (3.02 - h\nu) \text{ eV}, \tag{16a}$$

$$[CH_3I \cdots ICH_3] + h\nu \rightarrow I_2 + C_2H_6, \quad \Delta H = (-0.79 - h\nu) \text{ eV}. \tag{16b}$$

There are a number of difficulties with the sequential mechanisms. The endothermicity of reaction (15a) is too large to be surmounted by the translational energy release of $I(^2P_{3/2})$ (Table 1). Most of the excess energy from photodissociation is lost to CH_3 translation energy. Reaction (15b) is exothermic, however, I^* is rapidly quenched to I in collisions with CH_3I [32]. Also $I + I^*$ does not correlate with the ground electronic state of I_2. However, curve crossings are possible, especially if a cage effect involving the two I atoms is involved. So this reaction cannot be eliminated from consideration. The recombination of $2CH_3$ to form C_2H_6 can be an

important driving force toward I_2 formation. This mechanism is operative in larger clusters both in the gas phase [19] and in matrices [34]. However, it is difficult to imagine this recombination occurring in $(CH_3I)_2$ dimers unless the head-to-head geometry is highly bent, such as in an L shape. It is also possible that I_2 is not formed in dimers but in small clusters. The evidence for dimer reaction by the groups of Vaida [18], Donaldson [21], and in this work cannot rule out the involvement of trimers and larger. Unfortunately, the quantum yield for I_2 formation has not been measured, however, a relative yield of I_2 versus I escape should be possible in the future.

The concerted mechanism proposed by Donaldson and coworkers [21] is based on an exciton-like excitation wherein both C–I bonds break near-simultaneously (reaction (16a)). This mechanism would seem to require a photon energy sufficient to break both C–I bonds (2×2.30 eV or $\lambda < 266$ nm), which contradicts the observation here of I_2 at 304 nm; however, the potential surface for a concerted mechanism could conceivably involve a lower barrier. The energetics for a concerted mechanism are favorable without invoking an excitonic photolysis if the formation of ethane is involved (reaction (16b)). This mechanism is similar to the four-center reactions observed for $(HI)_2 \rightarrow I_2 + 2H$ (or H_2). Buntine et al. reported formation of H_2 from $(HI)_n$ photolysis, which they attribute to a four-center reaction involving dimer [35]. Polanyi and coworkers have postulated a similar mechanism for surface photochemistry of hydrogen halides [36]. However, as mentioned above for $(CH_3I)_n$ cluster studies, although dimer formation may dominate, the importance of higher clusters cannot be ruled out, even on surfaces.

The translational energy distributions measured here are consistent with cluster excitation involving monomer units rather than excitonic dimer states, since the latter cannot explain the relatively high translational energies observed. The present results provide new clues to the formation of I_2, but cannot reduce the possible mechanisms to a unique reaction. However, the present technique of measuring product angle velocity distributions, and for the case of diatomic and polyatomic fragments, the rovibrational distributions measurements, should provide important details. We plan to measure these properties for I_2 to determine product alignments and lifetimes.

5.4. Branching ratio

There are several possible explanations for the increase in the $^2P_{3/2}$ to $^2P_{1/2}$ branching ratio for cluster versus monomer dissociation seen in Fig. 10. First, I^* may preferentially react to give I_2 by reaction (15b) above. Second, because of the surface crossing in the *A* state that is responsible for the branching ratio in the monomer [37], it is possible that the increased production of $^2P_{3/2}$ is due to caging that allows the dissociation to proceed more adiabatically in the crossing region. Such a mechanism was invoked to explain an increased I/I^* branching ratio for CH_3I photodissociation on metal surfaces [27,28]. Third, the perpendicular transition moments that correlate with I dissociation, may be enhanced in the clusters due to symmetry breaking. Fourth, the $^2P_{1/2}$ state could be collisionally relaxed to $^2P_{3/2}$ as suggested above [32]. Finally, the $^2P_{1/2}$ state carries less translational energy and so may have a lower probability of escaping the cluster than the $^2P_{3/2}$ state. Future experiments will measure the branching ratio as a function of I atom velocity (as opposed to total ion detection used here) to answer this question.

6. Summary and conclusions

Angle velocity measurements of state selected photofragments from cluster excitation are sensitive probes of single and multiple collision interactions. In dimer systems, an initial alignment of collision partners defines a specific impact parameter. The present technique provides state resolved differential cross sections for specific scattering angles. In the near future, we plan to apply 2D sectional imaging [22] to record state resolved flux–velocity contour maps for bimolecular reactive scattering in photodissociated van der Waals aligned dimers. The scattering properties of the products can be interpreted to obtain the potential energy surface along the reaction coordinate. In this work, we showed that measurements of fragment angle velocity distributions can provide geometry information on the dimer. This is particularly true if the fragment pointing away from the dimer is measured. In larger cluster systems, the potential to explore energy relaxation by multiple

collisions, in analogy with condensed phase systems, becomes possible. Likewise, detailed information can be obtained concerning caging. In these experiments information is gained about the fragments that escape the cage, rather than the more common approach of following those fragments that recombine in the cage.

The study presented here concerns the direct photodissociation of CH_3I in clusters by excitation of the A state at 266 and 304 nm. Several interesting properties were measured including a fragment velocity dependent anisotropy, a bimodal I atom velocity distribution, an increased $^2P_{3/2}/^2P_{1/2}$ I atom spin–orbit distribution relative to gas phase CH_3I photodissociation, and detection of I atom from photodissociation of intracluster photoproduct I_2. These results are probing detailed reaction mechanisms in clusters. At this early stage of our work, the number of questions that are raised may well exceed the number that are answered. Many of these remaining issues are identified and additional experiments are described that should provide vital information. Perhaps, the greatest utility of the present technique, as applied to cluster dynamics, is that the experiments are routine and can be operated on standard molecular beam time-of-flight mass spectrometers.

Acknowledgements

This work was funded by the Aerospace Sponsored Research program.

References

[1] J.A. Syage, J. Phys. Chem. 99 (1995) 5772; in: Femtosecond chemistry, eds. J. Manz and L. Woeste (VCH Publishers, New York, 1995) p. 475, and references therein.

[2] S.K. Kim, J.J. Breen, D.M. Willberg, L.W. Peng, A. Heikal, J.A. Syage and A.H. Zewail, J. Phys. Chem. 99 (1995) 7421, and references therein; M.F. Hineman, G.A. Bruker, D.F. Kelley and E.R. Bernstein, J. Chem. Phys. 97 (1992) 3341.

[3] T. Baumert, S. Pedersen and A.H. Zewail, J. Phys. Chem. 97 (1993) 12447.

[4] C. Jouvet and B. Soep, Chem. Phys. Letters 96 (1983) 426; C. Jouvet, M. Boivineau, M.C. Duval and B. Soep, J. Phys. Chem. 91 (1987) 5416.

[5] C. Wittig, S. Sharpe and R.A. Beaudet, Accounts Chem. Res. 21 (1988) 341; S.K. Shin, Y. Chen, S. Nicholaisen, S.W. Sharpe, R.A. Beaudet and C. Wittig, Advan. Photochem. 16 (1991) 249, and references therein.

[6] S.I. Ionov, G.A. Bruker, C. Jaques, L. Valachovic and C. Wittig, J. Chem. Phys. 99 (1993) 6553.

[7] N.J. Scherer, L.R. Khundkar, R.B. Bernstein and A.H. Zewail, J. Chem. Phys. 87 (1987) 1451; N.F. Scherer, C. Sipes, R.B. Bernstein and A.H. Zewail, J. Chem. Phys. 92 (1990) 5239.

[8] J. Segall, Y. Wen, R. Singer, C. Wittig, A. Garcia-Vela and R.B. Gerber, Chem. Phys. Letters 207 (1993) 504; C. Jaques, L. Valachovic, S. Ionov, E. Bohmer, Y. Wen, J. Segall and C. Wittig, J. Chem. Soc. Faraday Trans. 89 (1993) 1419.

[9] J.S. Riley and T. Baer, Intern. J. Mass Spectrom. Ion Proc. 131 (1994) 295; K. Ohashi and N. Nishi, J. Chem. Phys. 98 (1993) 390; C.M. Roehl, J.T. Snodgrass, C.A. Deakyne and M.T. Bowers, J. Chem. Phys. 94 (1991) 6546, and references therein.

[10] R. Ogorzalek Loo, G.E. Hall, H.-P. Haerri and P.L. Houston, J. Phys. Chem. 92 (1988) 5.

[11] S.M. Penn, C.C. Hayden, K.J. Carlson Muyskens and F.F. Crim, J. Chem. Phys. 89 (1988) 2909.

[12] J.A. Syage, Chem. Phys. Letters 245 (1995) 605.

[13] M.A. Young, J. Chem. Phys. 102 (1995) 7925; J. Phys. Chem. 98 (1994) 7790.

[14] R.J. Bemish, E.J. Bohac, M. Wu and R.E. Miller, J. Chem. Phys. 101 (1994) 9457.

[15] D.M. Willberg, M. Gutmann, J.J. Breen and A.H. Zewail, J. Chem. Phys. 96 (1992) 198; M. Gutmann, D.M. Willberg and A.H. Zewail, J. Chem. Phys. 97 (1992) 8037, 8048.

[16] J.M. Papanikolas, V. Vorsa, M.E. Nadal, P.J. Campagnola, H.K. Buchenau and W.C. Lineberger, J. Chem. Phys. 99 (1993) 8733; D. Ray, N.E. Levinger, J.M. Papanikolas and W.C. Lineberger, J. Chem. Phys. 91 (1989) 6533.

[17] R. Zadoyan, P. Ashjian, Z. Li, C.C. Martens and V.A. Apkarian, Chem. Phys. Letters 218 (1994) 504; R. Zadoyan, Z. Li, C.C. Martens and V.A. Apkarian, J. Chem. Phys. 101 (1994) 6648.

[18] S.P. Sapers, V. Vaida and R. Naaman, J. Chem. Phys. 88 (1988) 3638.

[19] J.A. Syage and J. Steadman, Chem. Phys. Letters 166 (1990) 159.

[20] P.G. Wang, Y.P. Zhang, C.J. Ruggles and L.D. Zeigler, J. Chem. Phys. 92 (1990) 2806.

[21] K.L. Randall and D.J. Donaldson, J. Phys. Chem. 99 (1995) 6763; Y. Fan, K.L. Randall and D.J. Donaldson, J. Chem. Phys. 98 (1993) 4700; Y.B. Fan and D.J. Donaldson, J. Chem. Phys. 97 (1992) 189.

[22] R.A. Hertz and J.A. Syage, J. Chem. Phys. 100 (1994) 9265; J.A. Syage, J. Phys. Chem. 99 (1995) 16530; J.A. Syage, J. Chem. Phys., in press.

[23] R. Ogorzalek Loo, H.-P. Haerri, G.E. Hall and P.L. Houston, J. Chem. Phys. 90 (1989) 4222.

[24] H.J. Hwang and M.A. El-Sayed, J. Chem. Phys. 94 (1991) 4877; 96 (1992) 856.

[25] T.A. Spiglanin and D.W. Chandler, Chem. Phys. Letters 141 (1987) 428.
[26] J.A. Syage, J. Chem. Phys. 92 (1990) 1804.
[27] E.T. Jensen and J.C. Polanyi, J. Phys. Chem. 97 (1993) 2257.
[28] D.H. Fairbrother, K.A. Briggman, P.C. Stair and E. Weitz, J. Chem. Phys. 102 (1995) 7267.
[29] R.D. Clear and K.R. Wilson, J. Mol. Spectry. 47 (1973) 39; H.J. Hwang and M.A. El-Sayed, J. Phys. Chem. 95 (1991) 8044.
[30] S.J. Riley and K.R. Wilson, Faraday Discuss. Chem. Soc. 53 (1972) 132; W.P. Hess, S.J. Kohler, H.K. Haugen and S.R. Leone, J. Chem. Phys. 84 (1986) 2143.
[31] R.K. Sparks, K. Shobatake, L.R. Carlson and Y.T. Lee, J. Chem. Phys. 75 (1981) 3838; G.N.A. van Veen, T. Baller, A.E. de Vries and N.J.A. van Veen, Chem. Phys. 87 (1984) 405; M.D. Barry and P.A. Gorry, Mol. Phys. 52 (1984) 461.
[32] I.V. Hertel, Advan. Chem. Phys. 45 (1981) 341; S.L. Baughcum and S.R. Leone, J. Chem. Phys. 72 (1980) 6531; C. Fotakis and R.J. Donovan, J. Chem. Soc. Faraday Trans. 2 74 (1978) 2099.
[33] J.S. Muenter, J. Chem. Phys. 103 (1995) 1263.
[34] T. Momose, M. Miki, M. Uchida, T. Shimizu, I. Yoshizawa and T. Shida, J. Chem. Phys. 103 (1995) 1400.
[35] M.A. Buntine, D.P. Baldwin, R.N. Zare and D.W. Chandler, J. Chem. Phys. 94 (1991) 4672.
[36] C.-C. Cho, J.C. Polanyi and C.D. Stanners, J. Chem. Phys. 90 (1989) 598; E.B.D. Bourdon, C.-C. Cho, P. Das, J.C. Polanyi, C.D. Stanners and G.-Q. Xu, J. Chem. Phys. 95 (1991) 1361.
[37] M. Shapiro, J. Phys. Chem. 90 (1986) 3644; M. Trajeddine, J.P. Flament and C. Teichteil, Chem. Phys. 118 (1987) 45.